

# On the electron vortex beam wavefunction within a crystal

B.G. Mendis

*Dept. of Physics, Durham University, South Road, Durham, DH1 3LE, UK*

## Abstract

Electron vortex beams are distorted by scattering within a crystal, so that the wavefunction can effectively be decomposed into many vortex components. Using a Bloch wave approach equations are derived for vortex beam decomposition at any given depth and with respect to any frame of reference. In the kinematic limit (small specimen thickness) scattering largely takes place at the neighbouring atom columns with a local phase change of  $\pi/2$  radians. When viewed along the beam propagation direction only one vortex component is present at the specimen entrance surface (i.e. the ‘free space’ vortex in vacuum), but at larger depths the probe is in a mixed state due to Bragg scattering. Simulations show that there is no direct correlation between vortex components and the  $\langle L_z \rangle$  pendellösung, i.e. at a given depth probes with relatively constant  $\langle L_z \rangle$  can be in a more mixed state compared to those with more rapidly varying  $\langle L_z \rangle$ . This suggests that minimising oscillations in the  $\langle L_z \rangle$  pendellösung by probe channeling is not the only criterion for generating a strong electron energy loss magnetic circular dichroism (EMCD) signal.

*Keywords:* electron vortex beams, electron energy loss magnetic circular dichroism (EMCD), Bloch waves.

## 1.0 Introduction

Vortex beams are characterised by an azimuthal ( $\varphi$ ) phase dependence of the form  $\exp(im\varphi)$  and an expectation value of  $m\hbar$  for the  $\langle L_z \rangle$  orbital angular momentum, where  $m$  is the so-called winding number. The convention is to define the winding number with respect to a coordinate system where the beam propagation direction passes through its origin. For any other coordinate system the vortex wavefunction can effectively be decomposed into several vortex components with different winding numbers (defined with respect to the new coordinate system). This distinction becomes important in, for example, inelastic scattering of atoms at non-zero impact parameters, since the reference frame is usually defined with the atom nucleus at the origin [1-2]. In electron energy loss magnetic circular dichroism (EMCD) measurements this would mean that an off-centred vortex beam would be in a mixed state with respect to the excited atom, rather than being a pure vortex beam of  $\pm\hbar$  angular momentum (note that besides vortex beams there are other methods for measuring EMCD, such as using the crystal as a beam splitter [3]). Indeed Schattschneider *et al* [4] have shown that in order to detect a strong dichroic signal the vortex probe should be localised at the excited atom. A further complication is that even for a coordinate system centred about the beam propagation direction, the winding number is a constant of motion only when the electrostatic potential is either zero (free space propagation) or has cylindrical symmetry [5]. This condition is not satisfied for a zone-axis crystal, so that  $\langle L_z \rangle$  shows an oscillatory

pendellösung-type behaviour [5]. At sufficiently large depths therefore the vortex probe can be in a mixed state, even for zero impact parameter.

It has been proposed [6] that channeling of a  $m = \pm 1$  vortex can be induced by matching the wavefunction at the specimen entrance surface to the p-type Bloch states. This is similar to coupling of a conventional (i.e.  $m=0$ ) focussed probe to the 1s Bloch state localised at the atom columns. The channeling leads to smaller variations in the  $\langle L_z \rangle$  pendellösung. Bloch wave simulations [7] have shown that channeling is indeed enhanced when there is significant overlap between the vortex and p-type Bloch state wavefunctions at the specimen entrance surface. This is due to suppressing the 1s Bloch state excitation, which would otherwise give rise to short wavelength oscillations in  $\langle L_z \rangle$  through interference with other non-1s Bloch states that have a large difference in kinetic energy compared to 1s. Once the 1s state is suppressed the remaining oscillations in  $\langle L_z \rangle$  are due to interference between the non-1s states making up the probe. These oscillations are of long wavelength owing to similar kinetic energies [7], and hence  $\langle L_z \rangle$  is more slowly varying with respect to specimen depth.

Although the  $\langle L_z \rangle$  pendellösung is relatively well understood, there has been less work on the evolution of the vortex electron wavefunction as it propagates through a crystal (a notable exception is the topological study by Lubk *et al* [8]). In this paper the distortion of the vortex wavefunction due to scattering within a zone-axis crystal is analysed in more detail. A Bloch wave method is adopted, since the electron wavefunction at a given depth is mathematically more tractable than (say) multislice, so that decomposition into vortex components is straightforward (note however that Bloch wave and multislice results are identical). The results are also discussed in the context of EMCD measurements.

## 2.0 Simulation method

The vortex wavefunction within the probe forming aperture has the form  $A(\mathbf{k}_t)\exp(im\Phi)$ , where  $\mathbf{k}_t$  is the transverse component of the incident wavevector of azimuthal angle  $\Phi$ .  $A(\mathbf{k}_t)$  is unity for all  $\mathbf{k}_t$  within the aperture and zero outside it. The real space wavefunction within the specimen can then be expressed using Bloch waves [7]:

$$\psi(\mathbf{R}, z) = \beta \int A(\mathbf{k}_t) e^{im\Phi} \left\{ \sum_{j, \mathbf{g}} \varepsilon_o(\mathbf{k}_t) C_{\mathbf{g}}(\mathbf{k}_t) e^{2\pi i \mathbf{g} \cdot \mathbf{R}} e^{2\pi i \gamma z} \right\} e^{2\pi i \mathbf{k}_t \cdot (\mathbf{R} - \mathbf{R}_o)} d\mathbf{k}_t \quad (1)$$

where the  $j^{\text{th}}$ -Bloch wave has excitation  $\varepsilon_o$ , coefficients  $C_{\mathbf{g}}$  and change in longitudinal wavevector  $\gamma$  for illumination by a conventional (i.e.  $m=0$ ) plane wave of transverse wavevector  $\mathbf{k}_t$ .  $\beta$  is a normalisation constant for the electron intensity and the summation in Eq. (1) is carried out with respect to all Bloch states ( $j$ ) and reciprocal vectors ( $\mathbf{g}$ ). Real space coordinates are expressed as  $(\mathbf{R}, z)$ , where  $z$  is the depth within the specimen ( $z = 0$  corresponds to the specimen entrance surface) and  $\mathbf{R}$  is a two-dimensional position vector normal to the optic axis. The probe is incident at  $\mathbf{R}_o$ . Eq. (1) is similar to the wavefunction of

a conventional ( $m = 0$ ) focussed electron probe apart from the additional phase term  $\exp(im\Phi)$ , arising from the boundary conditions of the problem, i.e. the unscattered beam has unit amplitude and phase  $m\Phi$ . Eq. (1) assumes zero electron optic aberrations in the probe forming lens. Furthermore, inelastic scattering, particularly thermal diffuse scattering (TDS), is also ignored. In Bloch wave calculations TDS is modelled phenomenologically by introducing an imaginary term to the crystal potential [9]. This causes depletion of the elastic wavefield, thereby distorting calculated values of the  $\langle L_z \rangle$  angular momentum (see below). Many of the specimen depths considered in this study are however relatively small (e.g.  $\leq 200 \text{ \AA}$ ), so that TDS should have only a secondary effect.

$m = 1$  vortex probes with 10 and 30 mrad semi-convergence angle are simulated at 200 kV. The sample is [100]-oriented, body centred cubic Fe. At the specimen entrance surface the 30 mrad vortex probe has a similar wavefunction to the 2p-type Bloch states in [100]-Fe, while the 10 mrad probe is significantly broader [7; see also Fig. 3a]. The simulation included 121 Bloch states and 276, 648 partial plane waves ( $\mathbf{k}_l$ ) for the 10 and 30 mrad probes respectively. Doyle-Turner atom scattering factors are used. Convergence was confirmed by comparing the Bloch wave solution (Eq. 1) at the specimen entrance surface to the free space wavefunction of the focussed vortex probe [7,10; see also Eq. (8) in section 3.1 of this paper]. The  $\langle L_z \rangle$  angular momentum at a given depth was calculated using the following equation:

$$\langle L_z \rangle = -i\hbar \int \psi^* \frac{\partial \psi}{\partial \varphi} d\tau \quad (2)$$

where  $\varphi$  is the azimuthal angle in real space and  $d\tau$  is an infinitesimal area element perpendicular to the optic axis. For the 10 mrad probe Eq. (2) was evaluated over a  $6 \text{ \AA}$  radius (centred about the beam incident position) at  $0.2 \text{ \AA}$  spatial resolution, while for the 30 mrad probe the relevant parameters are a  $4 \text{ \AA}$  radius and  $0.07 \text{ \AA}$  spatial resolution. The finite sampling of the wavefunction meant that the calculated  $\langle L_z \rangle$  value at the specimen entrance surface was slightly different from the true value of  $\hbar$ , but the difference is sufficiently small not to affect the fundamental physics.

## 3.0 Results

### 3.1 Vortex beam decomposition

In this section equations are derived for decomposing a vortex wavefunction within a crystal into component states with respect to any given frame of reference. For convenience a ‘centred frame of reference’ is used to denote a coordinate system where the beam propagation direction passes through its origin, while all other frames are referred to as being ‘displaced’. Consider first a centred frame of reference (i.e.  $\mathbf{R}_0 = 0$ ). If  $k$  and  $R$  are the absolute values of  $\mathbf{k}_l$  and  $\mathbf{R}$ , then Eq. (1) becomes:

$$\psi(\mathbf{R}, z) = \beta \int A(\mathbf{k}_t) e^{im\Phi} \left\{ \sum_{j, \mathbf{g}} \varepsilon_o(\mathbf{k}_t) C_{\mathbf{g}}(\mathbf{k}_t) e^{2\pi i \mathbf{g} \cdot \mathbf{R}} e^{2\pi i \gamma z} \right\} e^{2\pi i k R \cos(\varphi - \Phi)} d\mathbf{k}_t \quad (3)$$

Using the identity for plane wave expansion into cylindrical harmonics [11]:

$$e^{iz \cos \theta} = \sum_{n=-\infty}^{\infty} i^n J_n(z) e^{in\theta} \quad (4)$$

where  $J_n$  is a  $n^{\text{th}}$ -order Bessel function of the first kind, it follows that by expanding the plane wave  $\exp[2\pi i k R \cos(\varphi - \Phi)]$  in Eq. (3), the vortex component with ‘winding number’  $l$  has the form:

$$\psi_l(\mathbf{R}, z) = i^l e^{il\varphi} \int \left\{ \sum_{j, \mathbf{g}} \varepsilon_o(\mathbf{k}_t) C_{\mathbf{g}}(\mathbf{k}_t) e^{2\pi i \mathbf{g} \cdot \mathbf{R}} e^{2\pi i \gamma z} \right\} e^{i(m-l)\Phi} J_l(2\pi k R) d\mathbf{k}_t \quad (5)$$

where  $\beta$  and  $A(\mathbf{k}_t)$  have been omitted from Eq. (5) and all subsequent equations for convenience. Note that the non-rigorous use of ‘winding number’ here is based on the  $\exp(il\varphi)$  phase term in Eq. (5), and does not follow the strict topological definition [8] (there is however no discrepancy in terminology at the specimen entrance surface). The term within the curly brackets is more conveniently expressed via the diffracted beam amplitudes  $\phi_{\mathbf{g}}(z)$ , which can be related to Bloch state parameters through the following equation [9]:

$$\phi_{\mathbf{g}}(z) = \sum_j \varepsilon_o C_{\mathbf{g}} \exp(2\pi i \gamma z) \quad (6)$$

Eq. (6) must be evaluated separately for each  $\mathbf{k}_t$  within the probe forming aperture. Substituting in Eq. (5) it follows that:

$$\psi_l(\mathbf{R}, z) = i^l e^{il\varphi} \int \phi_0(z) e^{i(m-l)\Phi} J_l(2\pi k R) d\mathbf{k}_t + i^l e^{il\varphi} \sum_{\mathbf{g} \neq \mathbf{0}} \int \phi_{\mathbf{g}}(z) e^{2\pi i \mathbf{g} \cdot \mathbf{R}} e^{i(m-l)\Phi} J_l(2\pi k R) d\mathbf{k}_t \quad (7)$$

The first and second terms represent the unscattered and scattered contributions respectively. At the specimen entrance surface  $\phi_0 = 1$  and  $\phi_{\mathbf{g}} = 0$  for all  $\mathbf{k}_t$ , so that only the first term remains. A non-zero value for the integral is only obtained when  $l=m$  (as required), and the resulting wavefunction is that for a focussed vortex probe in free space [10], i.e.:

$$\psi_m(\mathbf{R}, 0) = i^m e^{im\varphi} \int J_m(2\pi k R) d\mathbf{k}_t = 2\pi i^m e^{im\varphi} \int k J_m(2\pi k R) dk$$

(8)

Consider now the wavefunction with respect to a displaced frame of reference. The vortex centre, displaced frame of reference and electron wavefunction at point  $\mathbf{R}$  are related geometrically by a triangle as shown schematically in Figure 1. For convenience, and without loss of generality, the azimuthal angle  $\varphi$  is defined with respect to the axis joining the vortex centre and origin of the displaced coordinate system. If the azimuthal angle is further defined in a counter-clockwise sense, then the azimuthal angle for point  $\mathbf{R}$  with respect to the displaced frame is  $\theta$ . The Bessel addition theorem [11] states that for the triangle in Fig. 1:

$$e^{i\varphi} J_l(2\pi kR) = \sum_{n=-\infty}^{\infty} J_n(2\pi k\rho) J_{n+l}(2\pi kx) e^{in\alpha} \quad (9)$$

The total wavefunction in the centred frame is obtained by summing Eq. (5) over all integer  $l$ -values. Substituting Eq. (9) in the total wavefunction and grouping together all terms containing  $J_l(2\pi k\rho)$  gives:

$$\psi'_l(\mathbf{R}, z) = e^{il\alpha} \int \left\{ \sum_{j, \mathbf{g}} \varepsilon_o(\mathbf{k}_l) C_{\mathbf{g}}(\mathbf{k}_l) e^{2\pi i \mathbf{g} \cdot \mathbf{R}} e^{2\pi i \gamma z} \right\} \left\{ \sum_{p=-\infty}^{\infty} J_{p+l}(2\pi kx) i^p e^{-ip\Phi} \right\} e^{im\Phi} J_l(2\pi k\rho) d\mathbf{k}_l \quad (10)$$

Since  $i^p = \exp(ip\pi/2)$  the summation within the second curly brackets can be simplified by using the identity [11]:

$$\exp\left[\frac{z}{2}\left(t - \frac{1}{t}\right)\right] = \sum_{n=-\infty}^{\infty} J_n(z) t^n \quad (11)$$

With  $t = \exp[i(\pi/2 - \Phi)]$  it follows that:

$$\psi'_l(\mathbf{R}, z) = \frac{e^{il\alpha}}{i^l} \int \left\{ \sum_{j, \mathbf{g}} \varepsilon_o(\mathbf{k}_l) C_{\mathbf{g}}(\mathbf{k}_l) e^{2\pi i \mathbf{g} \cdot \mathbf{R}} e^{2\pi i \gamma z} \right\} e^{i[(m+l)\Phi + 2\pi kx \cos \Phi]} J_l(2\pi k\rho) d\mathbf{k}_l \quad (12)$$

Replacing  $l$  with  $-l$  and substituting  $\alpha = \pi - \theta$  (Fig. 1) gives:

$$\psi'_{-l}(\mathbf{R}, z) = \psi_l(\boldsymbol{\rho}, z) = i^l e^{i\theta} \int \left\{ \sum_{j, \mathbf{g}} \varepsilon_o(\mathbf{k}_l) C_{\mathbf{g}}(\mathbf{k}_l) e^{2\pi i \mathbf{g} \cdot \mathbf{R}} e^{2\pi i \gamma z} \right\} e^{i[(m-l)\Phi + 2\pi kx \cos \Phi]} J_l(2\pi k\rho) d\mathbf{k}_l \quad (13)$$

where the substitution  $J_{-l}(z) = (-1)^l J_l(z)$  valid for integer  $l$ , has been made [11]. Eq. (13) has the correct azimuthal dependence for a vortex state of ‘winding number’  $l$  with respect to the displaced frame of reference. Hence in order to simplify the terminology  $\psi'_{-l}(\mathbf{R}, z)$  will be replaced by  $\psi_l(\mathbf{p}, z)$  for displaced frames. Eq. (13) can also be represented using diffracted beam amplitudes:

$$\psi_l(\mathbf{p}, z) = i^l e^{il\theta} \int \phi_0(z) e^{i[(m-l)\Phi + 2\pi kx \cos\Phi]} J_l(2\pi k\rho) d\mathbf{k}_l + i^l e^{il\theta} \sum_{\mathbf{g} \neq 0} \int \phi_{\mathbf{g}}(z) e^{2\pi i \mathbf{g} \cdot \mathbf{R}} e^{i[(m-l)\Phi + 2\pi kx \cos\Phi]} J_l(2\pi k\rho) d\mathbf{k}_l \quad (14)$$

At the specimen entrance surface only the first term remains, i.e.:

$$\psi_l(\mathbf{p}, 0) = i^l e^{il\theta} \int \int e^{i[(m-l)\Phi + 2\pi kx \cos\Phi]} d\Phi \int k J_l(2\pi k\rho) dk \quad (15)$$

The azimuthal integral can be simplified using the integral representation of a Bessel function [11], i.e.:

$$J_n(z) = \frac{1}{2\pi} \int_{-\pi}^{\pi} e^{i(-nt + z \sin t)} dt \quad (16)$$

so that Eq. (15) becomes:

$$\psi_l(\mathbf{p}, 0) = 2\pi i^m e^{il\theta} \int k J_{m-l}(2\pi kx) J_l(2\pi k\rho) dk \quad (17)$$

As  $x \rightarrow 0$  non-zero components are only obtained when  $l=m$  due to the  $J_{m-l}(2\pi kx)$  Bessel term and Eq. (17) converges to the vortex wavefunction with respect to a centred frame (Eq. 8) as required (note that  $\theta \approx \varphi$  for small  $x$ ). For non-zero values of  $x$  the wavefunction can be decomposed into vortex components with  $l \neq m$ . However, the  $J_{m-l}(2\pi kx)$  term requires that the allowed  $l$ -values are grouped around  $m$ , the spread in  $l$ -values depending on the aperture size. For small apertures only  $l$ -values close to  $m$  are allowed, but this condition is relaxed as the aperture size increases. As  $x$  diverges however the excitation of vortex components is suppressed as required, due to the asymptotic value of the Bessel function being zero [11].

### 3.2 Scattering within the crystal- kinematic limit and dynamic diffraction

Equations (5) and (13), or equivalently equations (7) and (14), represent decomposition of a vortex wavefunction into individual components with respect to centred and displaced frames of reference respectively. Due to scattering decomposition of the wavefunction within the crystal is different to the specimen entrance surface. This section presents results for 200 kV,

$m = 1$  vortex probes with 10 and 30 mrad semi-convergence angles in [100]-Fe as a model system.

First consider the kinematic limit, where  $\phi_0$  is approximately unity and  $\phi_g$  are small. For a centred frame of reference Eq. (7) therefore becomes:

$$\psi_l(\mathbf{R}, z) \approx i^l e^{il\varphi} \int e^{i(m-l)\Phi} J_l(2\pi kR) d\mathbf{k}_t + i^l e^{il\varphi} \sum_{\mathbf{g} \neq 0} \int \phi_g(z) e^{2\pi i \mathbf{g} \cdot \mathbf{R}} e^{i(m-l)\Phi} J_l(2\pi kR) d\mathbf{k}_t \quad (18)$$

If the specimen is treated as a phase object an incident plane wave undergoes a phase change  $\exp[i\sigma V_p(\mathbf{R})]$ , where  $\sigma$  is the interaction constant and  $V_p$  the projected potential [12]. For weak phase objects the wavefunction is therefore:

$$\psi(\mathbf{R}, z) = \exp(2\pi i \mathbf{k}_t \cdot \mathbf{R}) \exp[i\sigma V_p(\mathbf{R})] \exp(2\pi i k_z z) \approx \exp(2\pi i \mathbf{k}_t \cdot \mathbf{R}) [1 + i\sigma V_p(\mathbf{R})] \exp(2\pi i k_z z) \quad (19)$$

where  $k_z$ ,  $\mathbf{k}_t$  are the longitudinal wavevector component and transverse wavevector of the incident plane wave respectively. The wavefunction may also be expressed in terms of the diffracted beam amplitudes [9]:

$$\begin{aligned} \psi(\mathbf{R}, z) &= \left\{ \phi_0(z) \exp(2\pi i \mathbf{k}_t \cdot \mathbf{R}) + \sum_{\mathbf{g} \neq 0} \phi_g(z) \exp[2\pi i (\mathbf{k}_t + \mathbf{g}) \cdot \mathbf{R}] \right\} \exp(2\pi i k_z z) \\ &\approx \exp(2\pi i \mathbf{k}_t \cdot \mathbf{R}) \left\{ 1 + \sum_{\mathbf{g} \neq 0} \phi_g(z) \exp(2\pi i \mathbf{g} \cdot \mathbf{R}) \right\} \exp(2\pi i k_z z) \end{aligned} \quad (20)$$

Comparing Eqs. (19) and (20) it follows that for a weak phase object  $\sum \phi_g \exp(2\pi i \mathbf{g} \cdot \mathbf{R}) = i\sigma V_p(\mathbf{R})$ , so that Eq. (18) simplifies to:

$$\psi_l(\mathbf{R}, z) \approx i^l e^{il\varphi} \int e^{i(m-l)\Phi} J_l(2\pi kR) d\mathbf{k}_t + i^{l+1} e^{il\varphi} \sigma \int V_p(\mathbf{R}) e^{i(m-l)\Phi} J_l(2\pi kR) d\mathbf{k}_t \quad (21)$$

The scattered vortex wavefunction peaks at the atom columns where  $V_p(\mathbf{R})$  is maximum and is phase shifted by  $\pi/2$  radians with respect to the unscattered vortex. This is illustrated in Figure 2 which maps the intensity and phase for the 200 kV,  $m = 1$ , 10 mrad vortex probe in [100]-Fe at the specimen entrance surface and at a depth of 10 Å respectively. The vortex probe is incident along the atom column in the centre of the image and the wavefunction was calculated using Eq. (1). Note that the phase plots (Figs. 2b and 2d) show some distortion due to the use of a finite set of Bloch waves. This is especially true at points where the phase changes abruptly from  $2\pi$  to 0 radians and regions of low electron intensity. The main conclusions in this paper are however not affected by this numerical error. From Fig. 2d the

phase has shifted by approximately  $\pi/2$  radians at the nearest neighbour atom columns at 10 Å depth, but is relatively unchanged in the low potential regions (apart from a trivial phase advance due to propagation over a 10 Å distance). A further observation is that even though the electron intensity at the specimen entrance surface is relatively weak at the nearest neighbour atom columns (Fig. 2a), at 10 Å depth the intensity is attracted towards the columns due to their focussing effect [13]. Since vortex beam distortion is largely caused by scattering at the atom columns, it is important that the wavefunction at the specimen entrance surface does not overlap (or is close to overlapping) with any atom columns. This effectively suppresses the 1s Bloch state excitation; the relatively wide separation in  $\gamma$ -value between the 1s state and other non-1s states means that their interference produces rapidly oscillating changes in the wavefunction (especially at the atom column positions) and hence  $\langle L_z \rangle$  with respect to depth [7]. Finally the weak phase object result from Eq.(21), where scattering by  $V_p(\mathbf{R})$  gives rise to a phase shifted vortex, can be extended to displaced frames of references as well (i.e. Eq. 14), and is therefore a general property of vortex beams.

At larger specimen thicknesses a full dynamical scattering calculation must be carried out. Figure 3a shows the radial intensity profiles at the specimen entrance surface for the 200 kV,  $m = 1$  vortex probes with 10 and 30 mrad semi-convergence angles (the peak intensity has been normalised for direct comparison). The 30 mrad probe has maximum intensity at only  $\sim 0.3$  Å away from the vortex centre, while the 10 mrad probe is significantly more delocalised. The convergence angle has a considerable influence on the  $\langle L_z \rangle$  pendellösung, as shown in Figure 3b for the case of a vortex probe incident on an atom column in [100]-Fe.  $\langle L_z \rangle$  oscillations are larger for the 10 mrad probe due to interference of the 1s Bloch state with other non-1s states [7]. Excitation of the 1s state is however suppressed for the narrower 30 mrad probe, so that the  $\langle L_z \rangle$  value varies less during probe propagation.

Consider first the scenario where a vortex probe is incident on an atom column in [100]-Fe. At the specimen entrance surface there is only the  $l=m=1$  vortex component with respect to a centred frame of reference (Eq. 7). Within the specimen Bragg scattering results in non-zero values for  $\phi_{\mathbf{g}}$ , while  $\phi_0$  deviates from unit amplitude. From Eq. (7) this means that  $l \neq m$  vortex components can be generated within the crystal (w.r.t. a centred fame), especially at large depths where diffraction is strong. The redistribution of intensity between the Bragg beams is however strongest when the incident wave vector is at the Bragg angle, i.e.  $l \neq m$  vortex components are not uniformly generated within the probe forming aperture, but certain  $\mathbf{k}_l$  have a larger effect than others. Figures 3c and 3d show the transmitted intensity and total diffracted intensity as a function of depth for the 10 and 30 mrad vortex probes respectively. The intensities are normalised with respect to the probe intensity. For both probes the total diffracted intensity ‘saturates’ by  $\sim 150$  Å depth, so that the wavefunction should be in a highly mixed state at these depths. The decomposition into vortex components (centred frame) at depths of  $z = 0, 50, 230$  and  $420$  Å are shown in Figure 4 for the 10 mrad probe and Figure 5 for the 30 mrad probe. The non-zero values for depth were selected based on the fact that they correspond to maxima in the diffracted intensity pendellösung for the 10 mrad probe (Fig. 3c). In Figs. 4 and 5 the integrated intensity for each of the vortex components is plotted at the relevant depth. As expected the wavefunction is in a highly mixed state at 230 and 420

Å depths (Figs. 4c-d and 5c-d), although for the 10 mrad probe the  $l = 1$  vortex state is still largely the dominant component. The allowed components are distributed either side of the incident vortex winding number (i.e.  $m = 1$ ); components for which  $|m-l|$  is relatively large are damped by the rapidly varying  $\exp[i(m-l)\Phi]$  phase term in Eq. (7). It is somewhat surprising that within the specimen the 30 mrad probe is in a more mixed state compared to the 10 mrad probe, despite the former showing much less variation in the  $\langle L_z \rangle$  pendellösung (Fig. 3b).

The results can be discussed in the context of EMCD measurements. For accurate measurements an orbital angular momentum of  $+\hbar$  ( $-\hbar$ ) must be transferred from the  $m = 1$  ( $m = -1$ ) vortex beam to the atom, so that the EMCD signal extracted from the difference in energy loss spectra for  $m = \pm 1$  beams is representative of the magnetic properties of the sample. An orbital angular momentum of  $+\hbar$  could potentially be transferred from the  $l = 1$  vortex component or any other component of higher ‘winding number’, and similarly for an orbital angular momentum transfer of  $-\hbar$  [1-2]. Since at larger depths the vortex probe is in a mixed state both types of transitions should be possible, thereby potentially distorting the EMCD signal. Rusz and colleagues [14-15] have used a combined multislice-Bloch wave approach to simulate the inelastic magnetic and non-magnetic signals as a function of vortex beam semi-convergence angle and specimen thickness in [100]-Fe. It was found that the relative strength of the magnetic signal (compared to the non-magnetic signal) typically decreased with specimen thickness [14], consistent with the above observation of a vortex probe in a mixed state. Interestingly for a given specimen thickness the relative strength of the magnetic signal peaked at a semi-convergence angle smaller than 30 mrad, which is the value required to match the  $m = 1$  vortex wavefunction at the specimen entrance surface to the [100]-Fe, p-type Bloch states [7], thereby inducing strong channeling. In most cases the optimum semi-convergence angle was found to be  $\sim 19$  mrad [14]. This suggests that minimising oscillations in the  $\langle L_z \rangle$  pendellösung alone is not sufficient for optimising the EMCD signal, but that decomposition of the probe into individual vortex components within the specimen must also be taken into account. In fact the 19 mrad probe was found to be in a less mixed state at depths of 50, 230 and 420 Å compared to the 30 mrad probe, but more mixed compared to the 10 mrad probe (centred frame; results not shown).

The  $l = 1$  vortex component wavefunction (centred frame) at 230 Å depth for the 10 mrad probe is shown in Figure 6. Figs. 6a and 6c show the intensity distribution for the unscattered and scattered parts of the wavefunction (i.e. the first and second terms of Eq. 7 respectively). The unscattered intensity is radially symmetric (as required by Eq. 7) and extends as far as the second nearest neighbour atom columns, even though at the specimen entrance surface the wavefunction is largely confined to within the first nearest neighbour columns (Fig. 2a). The interpretation for this broadening effect is straightforward. For a non-absorbing crystal  $\epsilon_0 = C_0^*$  [9], so that  $\phi_0$  in the unscattered wavefunction of Eq. (7) is  $\sum |\epsilon_0|^2 \exp(2\pi i \gamma z)$ . This effectively represents interference of the Bloch states in the vertical  $z$ -direction weighted by the square modulus of their excitation. In vacuum the  $z$ -dependence of a vortex probe with winding number  $m$  is given by [10,16]:

$$\psi_{\text{vac}}(\mathbf{R}, z) = 2\pi i^m e^{im\varphi} \int k e^{2\pi i k_z z} J_m(2\pi k R) dk \quad (22)$$

The free space vortex probe broadens either side of the  $z = 0$  focal plane due to the  $\exp(2\pi i k_z z)$  phase term [6]. Within the crystal however the  $z$ -dependence is modified to  $\Sigma|\varepsilon_{\theta}|^2 \exp(2\pi i \gamma z)$ , due to channeling of the excited Bloch states. Fig. 6b shows the 200 kV, 10 mrad,  $m=1$  vortex intensity at 230 Å depth in free space (Eq. 22), where a broadening similar to Fig. 6a is evident, although the exact details vary due to the difference between vacuum and sample (e.g. in Fig. 6b a bright inner ring is observed, which is not apparent in Fig. 6a).

The scattered wavefunction on the other hand has intensity maxima at the atom column positions (Fig. 6c), similar to the kinematic result. This is due to the  $\exp(2\pi i \mathbf{g} \cdot \mathbf{R})$  phase factor in Eq. (7), i.e. when  $\mathbf{R}$  is a lattice translation vector the phase is independent of  $\mathbf{g}$ , so that overall there is less destructive interference of the  $\phi_{\mathbf{g}}$  terms. Furthermore, for this particular example  $l = m$ , so that the  $\exp[i(m-l)\Phi]$  phase term is constant; however, for vortex components where  $(m-l)$  is non-zero simulations show that the scattered intensity need not be localised at the neighbouring atom columns. The wavefunction for the  $l=1$  component is due to the unscattered and scattered contributions, and its intensity and phase are shown in Figs. 6d and 6e respectively. At a depth of 230 Å the wavefunction is dominated by the scattered term, so that the intensity in this case is largely concentrated along the neighbouring atom columns and has a near constant phase for each column (Fig. 6e), which suggests that the intensity maxima are similar to atomic scale electron beams of zero winding number. The total electron intensity (Eq. 1) at 230 and 420 Å depths for the 200 kV,  $m=1$  vortex probes with 10 and 30 mrad semi-convergence angle are shown in Figure 7. For the 10 mrad probe a significant fraction of the intensity has been transferred to the neighbouring atom columns due to scattering. The scattered intensity is more delocalised for the 30 mrad probe, but nevertheless it is clear some of it has been transferred to the vicinity of the neighbouring atom columns. It is therefore important to analyse the role of nearest neighbour atom columns on the EMCD measurement, especially for relatively thick samples where scattering is dominant.

The EMCD signal from neighbouring atom columns must be analysed with respect to a displaced frame of reference with origin at the excited atom. Figures 8 and 9 respectively show the decomposition of the 10 and 30 mrad vortex probe wavefunctions into individual components at depths of  $z = 0, 50, 230$  and 420 Å; the decomposition is now with respect to a displaced frame of reference with origin at a nearest neighbour atom column. The graphs plot the integrated intensity of the vortex components at different depths. At the specimen entrance surface many vortex components are generated, the number of components increasing with the probe semi-convergence angle as required by Eq. (17). It is important to note however that as the nearest neighbour atom column distance decreases fewer vortex components are excited, until at zero distance only one vortex component (i.e.  $l=m$ ) is allowed at the specimen entrance surface. The nearest neighbour atom column distance in [100]-Fe is  $\sim 2$  Å, which is typical of most materials, so that excitation of multiple vortex

components at neighbouring atom columns is generally valid. This is true for non-zero depths as well (Figs. 8b-d and 9b-d). The simultaneous excitation of vortex components with  $\pm l$  ‘winding number’ (for small  $|m|$ , e.g.  $m = \pm 1$ ) at all depths *suggests* that neighbouring atom columns do not generate a strong EMCD signal, although (dichroism-free) inelastic scattering can still take place. Inelastic calculations are however required to confirm this, especially since from Eqs. (13), (14) the excitation of  $\pm l$  vortex components are not identical for  $m = \pm 1$ . Inelastic scattering is stronger for vortex components with relatively small values of  $|l|$ , since as  $|l|$  increases the peak intensity of the vortex is shifted further away from the atom. For probes with a large convergence angle many vortex components are excited with respect to a displaced frame of reference, so that the intensity of the small  $|l|$  components are diminished, thereby resulting in less inelastic scattering from neighbouring atom columns (e.g. from Figs. 8 and 9 the intensity of the vortex components are nearly an order of magnitude smaller for the 30 mrad probe compared to the 10 mrad probe). This is expected since a larger convergence angle produces a more localised vortex wavefunction.

#### 4.0 Summary and Conclusions

The above results can be summarised in the context of EMCD measurements. As a vortex beam of winding number  $m$  enters the crystal it is scattered by individual atom columns, leading to a localised phase shift of  $\pi/2$  radians. The wavefunction at shallow depths is dominated by the vortex component with winding number  $m$  (w.r.t. a centred frame), and an EMCD signal is generated from the atom column along which the probe is incident. Any EMCD (or indeed inelastic) signal from neighbouring atom columns decreases as the probe semi-convergence angle is increased. At larger specimen depths the electron beam is in a mixed vortex state due to dynamic scattering. The wavefunction of a vortex component at any given depth consists of an unscattered and scattered part. At larger depths the scattered part is sufficiently dominant to enable appreciable intensity to be transferred to the neighbouring atom columns. This has consequences for atomic scale EMCD measurements. However, it is not clear whether neighbouring atom columns can contribute a strong EMCD signal, since excitation of  $\pm l$  vortex components (as viewed by the neighbouring atom columns) could lead to a dichroism-free inelastic ‘background’ signal. A full inelastic calculation is nevertheless required to test this hypothesis. Finally no direct correlation was found between vortex beam decomposition and the  $\langle L_z \rangle$  pendellösung, which suggests that minimising variations in  $\langle L_z \rangle$  is not the only criterion for generating a strong EMCD signal.

#### 5.0 Acknowledgements

BGM would like to thank Durham University for granting research leave.

#### References

- [1] S. Lloyd, M. Babiker, and J. Yuan, Phys. Rev. Lett. **108**, 074802 (2012).
- [2] J. Yuan, S.M. Lloyd, and M. Babiker, Phys. Rev. A **88**, 031801 (2013).

- [3] P. Schattschneider, S. Rubino, C. Hébert, J. Ruzs, J. Kuneš, P. Novák, E. Carlino, M. Fabrizioli, G. Panaccione, and G. Rossi, *Nature* **441**, 486 (2006).
- [4] P. Schattschneider, S. Löffler, M. Stögger-Pollach, and J. Verbeeck, *Ultramicroscopy* **136**, 81 (2014).
- [5] S. Löffler, and P. Schattschneider, *Acta Cryst. A* **68**, 443 (2012).
- [6] H. Xin, and H. Zheng, *Microsc. Microanal.* **18**, 711 (2012).
- [7] B.G. Mendis, *Ultramicroscopy* **149**, 74 (2015).
- [8] A. Lubk, L. Clark, G. Guzzinati and J. Verbeeck, *Phys. Rev. A* **87**, 033834 (2013).
- [9] P.B. Hirsch, A. Howie, R.B. Nicholson, D.W. Pashley, and M.J. Whelan, *Electron Microscopy of Thin Crystals* (Butterworths, Great Britain, 1965).
- [10] P. Schattschneider, and J. Verbeeck, *Ultramicroscopy* **111**, 1461 (2011).
- [11] I.S. Gradshteyn, and I.M. Ryzhik, *Tables of Integrals, Series and Products*, Academic Press, New York, 1980.
- [12] J.C.H. Spence, *High-Resolution Electron Microscopy*, 3<sup>rd</sup> Edition (Oxford University Press, Oxford, 2003).
- [13] J. Fertig, and H. Rose, *Optik* **59**, 407 (1981).
- [14] J. Ruzs, S. Bhowmick, M. Eriksson and N. Karlsson, *Phys. Rev. B* **89**, 134428 (2014).
- [15] J. Ruzs and S. Bhowmick, *Phys. Rev. Lett.* **111**, (2013) 105504.
- [16] L. Xie, P. Wang, and X.Q. Pan, *Micron* **63**, 9 (2014).

## Figure captions

**Figure 1:** Schematic of the geometry between the vortex beam centre, origin of a displaced frame of reference and electron wavefunction at an arbitrary point  $\mathbf{R}$ . Equation (9) is based on a similar triangle to that shown in the figure, but with the sides magnified by a factor of  $2\pi k$ . See text for further details.

**Figure 2:** Intensity and phase (in radians) of a 200 kV, 10 mrad,  $m = 1$  vortex probe at the specimen entrance surface of [100]-Fe are shown in (a) and (b) respectively. The open circles represent individual atom columns and the vortex probe is incident along the atom column at the centre. The corresponding intensity and phase maps at 10 Å depth are shown in (c) and (d) respectively. Note that the phase shows some inaccuracy due to the use of a finite set of Bloch waves and regions of low electron intensity. The dimensions of each figure is 2x2 Å. Colour online.

**Figure 3:** (a) Radial intensity profiles at the specimen entrance surface for 200 kV,  $m = 1$  vortex beams with 10 and 30 mrad semi-convergence angles. The peak intensity has been normalised for direct comparison. The  $\langle L_z \rangle$  pendellösung (in units of  $\hbar$ ) for the 10 and 30 mrad probes incident along an atom column in [100]-Fe are shown in (b). (c) and (d) show the transmitted intensity (solid line) and total diffracted intensity (dashed line) pendellösung for the 10 and 30 mrad probes in [100]-Fe respectively. The intensities are normalised with respect to the incident probe intensity. Note the difference in depth scale between figures (b) and (c), (d).

**Figure 4:** Decomposition (w.r.t a centred frame) of a 200 kV, 10 mrad,  $m = 1$  vortex beam into individual components at depths of (a) 0 Å, (b) 50 Å, (c) 230 Å and (d) 420 Å in [100]-Fe. The vortex beam is incident along an atom column. The bars represent the integrated intensity of the vortex components. All graphs are plotted on the same vertical scale for direct comparison.

**Figure 5:** Decomposition (w.r.t a centred frame) of a 200 kV, 30 mrad,  $m = 1$  vortex beam into individual components at depths of (a) 0 Å, (b) 50 Å, (c) 230 Å and (d) 420 Å in [100]-Fe. The vortex beam is incident along an atom column. The bars represent the integrated intensity of the vortex components. All graphs are plotted on the same vertical scale for direct comparison.

**Figure 6:** (a) and (c) show the intensity distribution for the unscattered and scattered parts of the wavefunction (Eq. 7) for the  $l = 1$  vortex component at 230 Å depth in [100]-Fe w.r.t a centred frame. The original probe is a 200 kV, 10 mrad,  $m = 1$  vortex beam incident on an atom column. (d) and (e) show the intensity and phase (in radians) of the total wavefunction for the  $l = 1$  component at 230 Å depth. Note that the phase shows some inaccuracy due to the use of a finite set of Bloch waves and regions of low electron intensity. The intensity distribution for a 200 kV, 10 mrad,  $m = 1$  vortex beam at 230 Å depth in free space is shown in (b). The intensity has been normalised in figures (a) to (d), while the maximum intensity (arbitrary units) in figures (a), (c) and (d) are indicated in the inset for comparison. The open circles represent the atom column positions in [100]-Fe and each image has dimensions of  $4 \times 4$  Å. Colour online.

**Figure 7:** The intensity distribution for a 200 kV,  $m = 1$ , 10 mrad vortex probe at 230 and 420 Å depths in [100]-Fe are shown in (a) and (b) respectively. (c) and (d) are the corresponding images for the 30 mrad vortex probe. The open circles represent the atom column positions in [100]-Fe and the probe is incident along the central atom column. The image dimensions are  $4 \times 4$  Å for figures (a) and (b) and  $2 \times 2$  Å for figures (c) and (d). The maximum intensity in each image has been normalised. Colour online.

**Figure 8:** Decomposition (w.r.t a displaced frame with origin at a first nearest neighbour atom column) of a 200 kV, 10 mrad,  $m = 1$  vortex beam into individual components at depths of (a) 0 Å, (b) 50 Å, (c) 230 Å and (d) 420 Å in [100]-Fe. The vortex beam is incident along an atom column. The bars represent the integrated intensity of the vortex components. All graphs are plotted on the same vertical scale for direct comparison.

**Figure 9:** Decomposition (w.r.t a displaced frame with origin at a first nearest neighbour atom column) of a 200 kV, 30 mrad,  $m = 1$  vortex beam into individual components at depths of (a) 0 Å, (b) 50 Å, (c) 230 Å and (d) 420 Å in [100]-Fe. The vortex beam is incident along an atom column. The bars represent the integrated intensity of the vortex components. All graphs are plotted on the same vertical scale for direct comparison.

# Figures

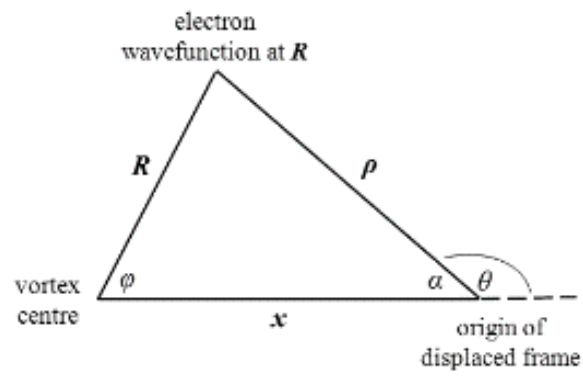


Figure 1

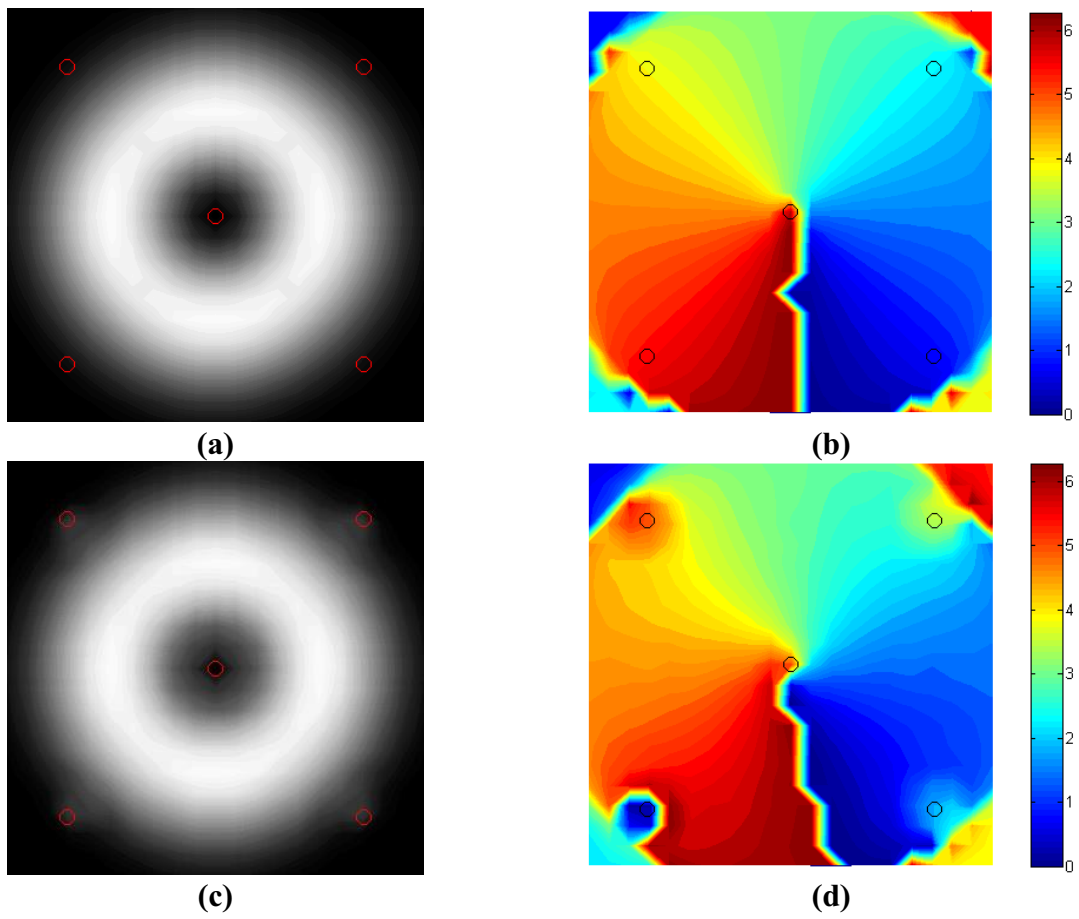
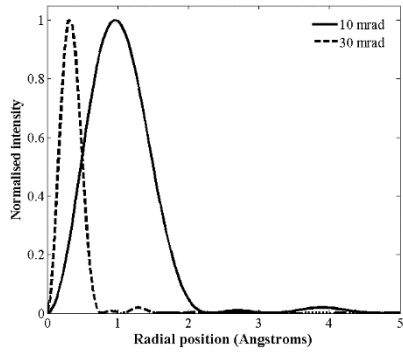
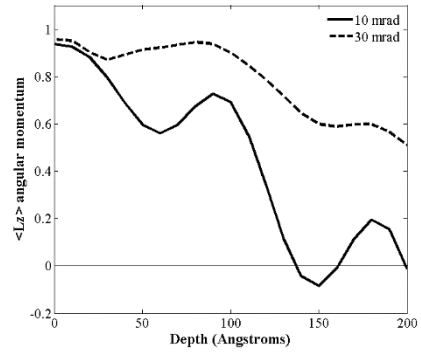


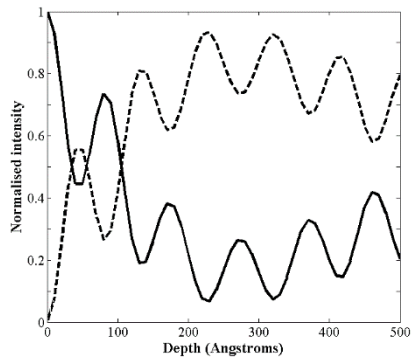
Figure 2



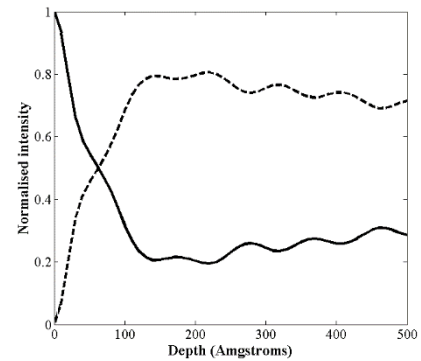
(a)



(b)

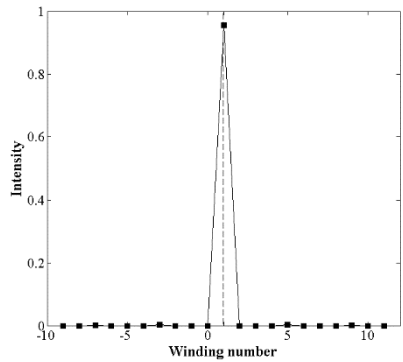


(c)

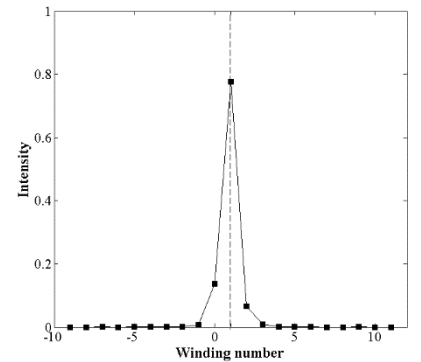


(d)

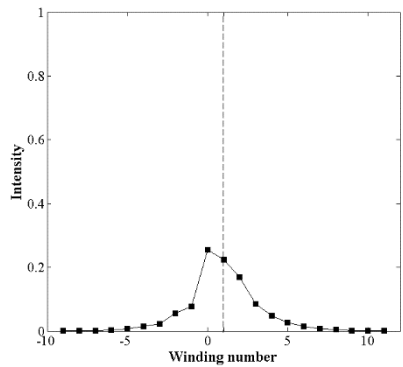
Figure 3



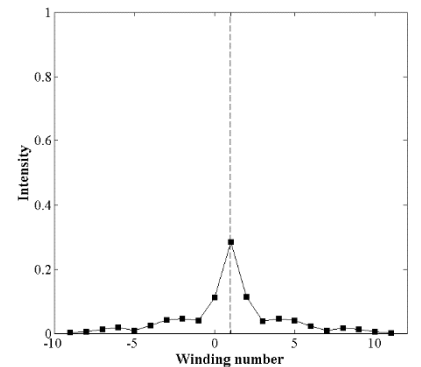
(a)



(b)

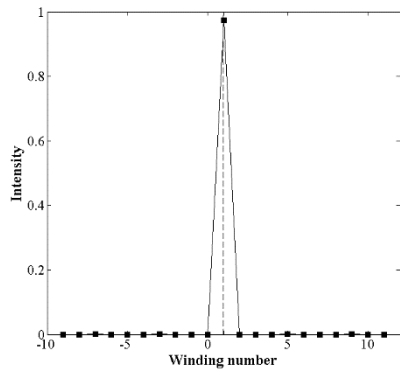


(c)

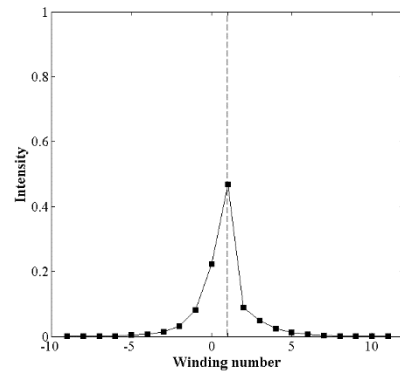


(d)

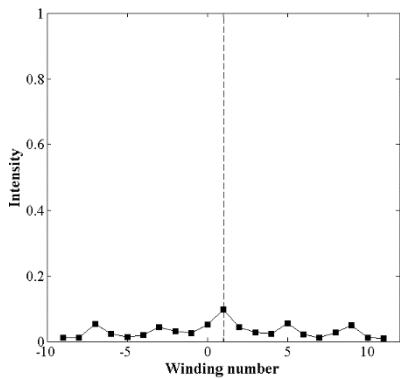
Figure 4



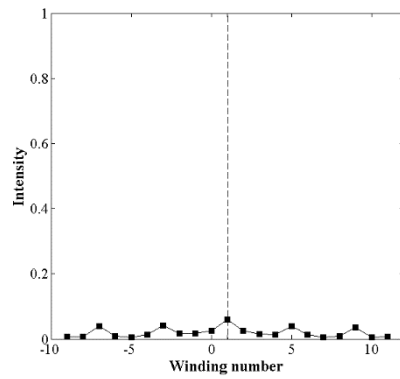
(a)



(b)

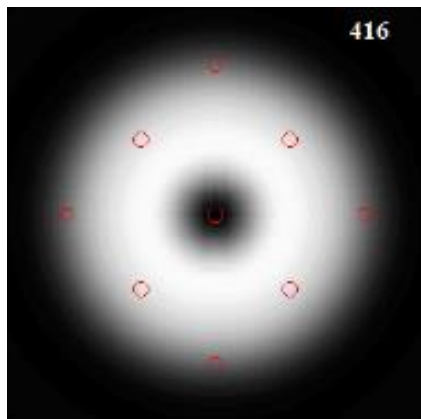


(c)

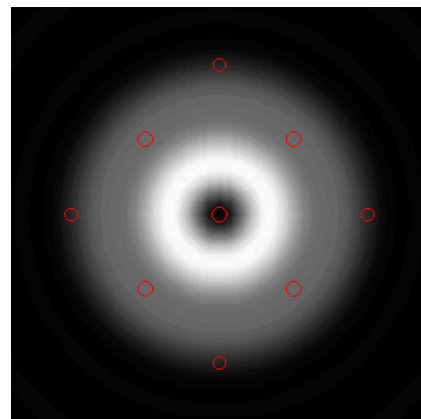


(d)

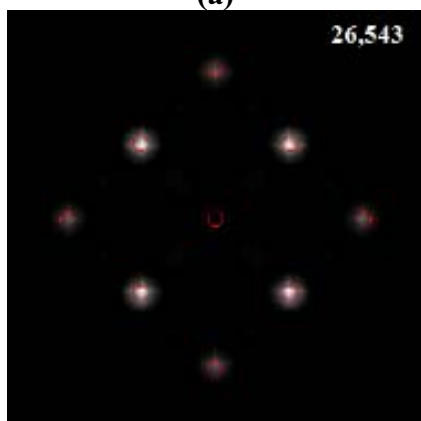
Figure 5



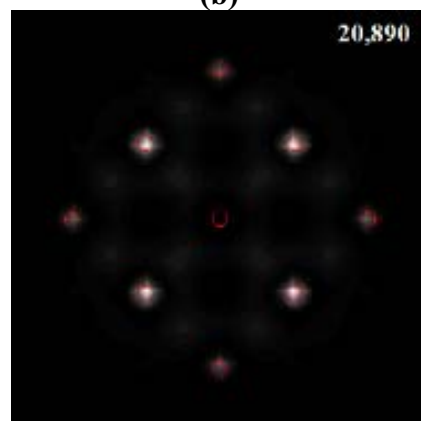
(a)



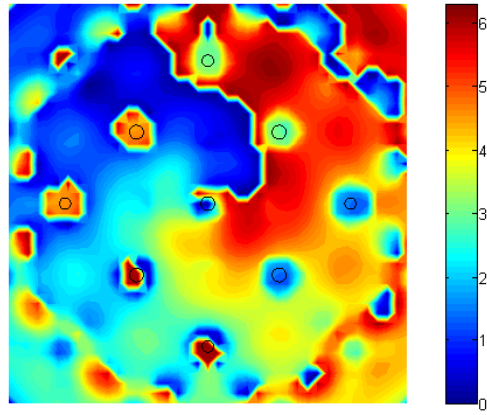
(b)



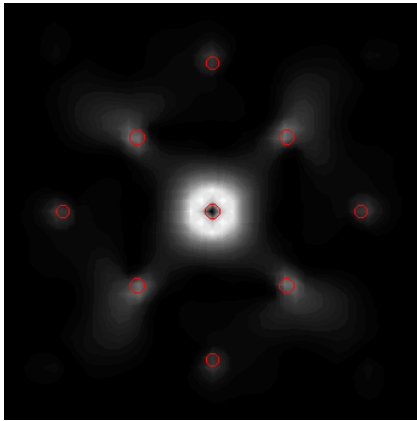
(c)



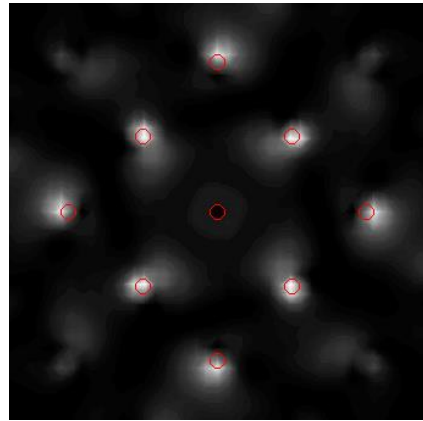
(d)



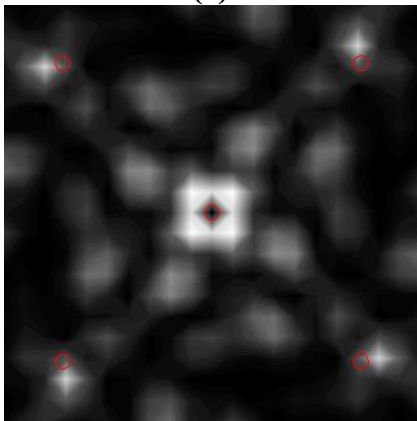
(e)  
Figure 6



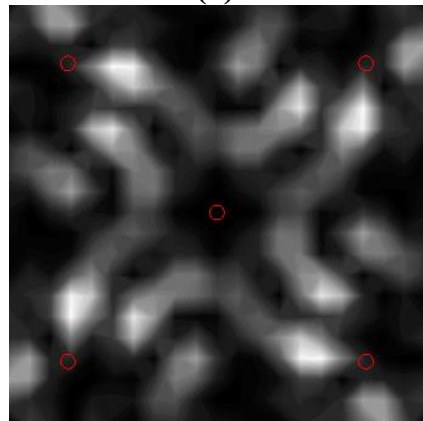
(a)



(b)

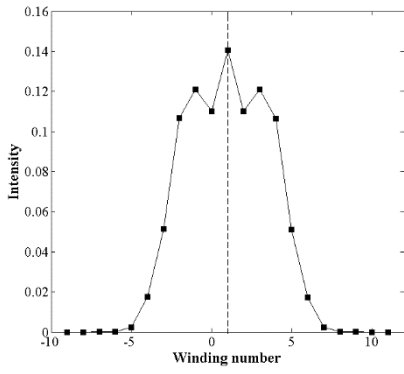


(c)

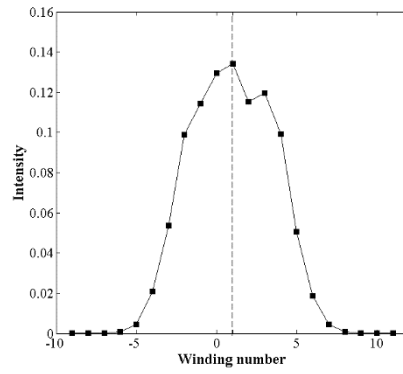


(d)

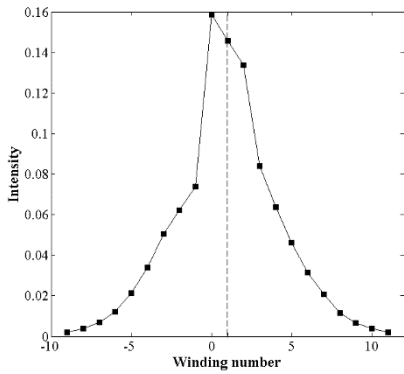
Figure 7



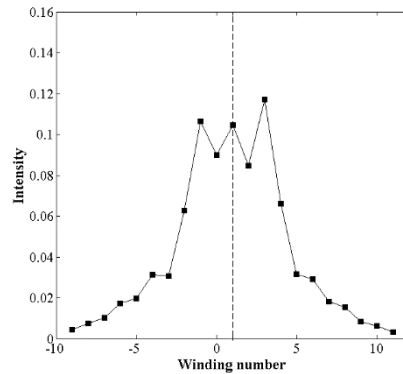
**(a)**



**(b)**

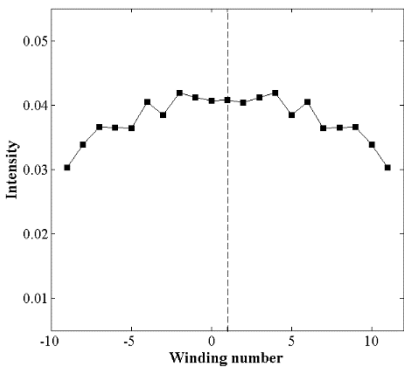


**(c)**

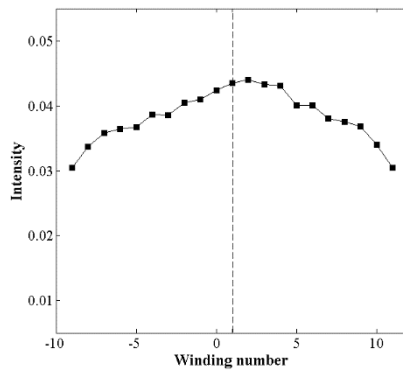


**(d)**

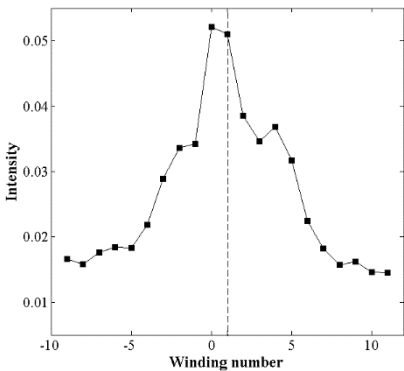
**Figure 8**



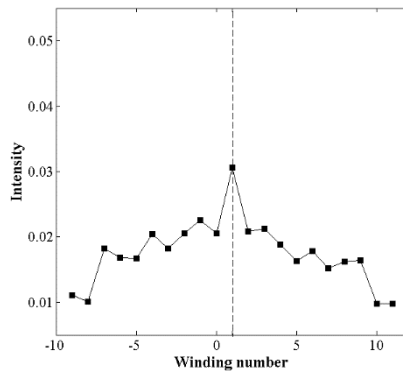
**(a)**



**(b)**



**(c)**



**(d)**

**Figure 9**